

Brittle and ductile fracture of semiconductor nanowires
— molecular dynamics simulations

Keonwook Kang and Wei Cai

Department of Mechanical Engineering

Stanford University, Stanford, CA 94305-4040, USA

November 9, 2006

Abstract

Fracture of silicon and germanium nanowires in tension at room temperature is studied by Molecular Dynamics simulations using several inter-atomic potential models. While some potentials predict brittle fracture initiated by crack nucleation from the surface, most potentials predict ductile fracture initiated by dislocation nucleation and slip. A simple parameter based on the ratio between the ideal tensile strength and the ideal shear strength is found to correlate very well with the observed brittle versus ductile behaviours for all the potentials used in this study. This parameter is then computed by *ab initio* methods, which predict brittle fracture at room temperature. A brittle-to-ductile transition (BDT) is observed in MD simulations at higher temperature. The BDT mechanism in semiconductor nanowires is different from that in the bulk, due to the lack of a pre-existing macrocrack that is always assumed in bulk BDT models.

keywords: fracture; brittle-to-ductile transition; semiconductor nanowires; Molecular Dynamics simulation; cracks; dislocations; nucleation

Contents

1	Introduction	3
2	Molecular dynamics simulations	4
2.1	Simulation method	4
2.2	Simulation results from SW potential	6
2.3	Simulation results from other potentials	7
2.4	Fundamental questions	9
3	Effect of inter-atomic potential models	9
3.1	Cut-off radius of inter-atomic potentials	9
3.2	Ideal tensile strength	10
3.3	Ideal shear strength and ductility parameter	12
4	Beyond empirical potential models	16
5	Brittle-to-ductile transition	17
5.1	Limitations of ductility parameter	17
5.2	MD observations	17
6	Summary	21
A	Alternative ductility indicators	26
B	Surface Reconstruction	28

1 Introduction

Directed growth of semiconductor nanowires (NWs) have attracted significant interest in recent years as key enablers of nanotechnology. With their diameter controllable by the size of the catalyst nanoparticles [1], and with their electronic properties tunable by doping [2], NWs can be used to construct nano-scale electronic devices, such as field effect transistors (FETs) [3, 4, 5], chemical and biological sensors [6], as well as nano-electrical-mechanical systems (NEMS) such as actuators [7] and nano-fluidic components [8]. Reliable functioning of these novel devices depends critically on the mechanical stability of the NWs and their contacts under processing and working conditions. Characterizing and predicting the mechanical strength of NWs is necessary because significant stress may build up due to the thermal or lattice mismatch, even though the primary function of these NWs is usually not to bear loads.

NWs are attractive systems for studying the fundamental deformation mechanisms of materials. Establishing a quantitative connection between the physics of defects and the mechanical properties of materials has been a dream of computational materials scientists for a long time. It remains a significant challenge because of the large gap in length scale between the two. The growing ability to fabricate and mechanically test high-quality micro- and nano-scale specimens presents a unique opportunity to close this gap, as computer simulations of defect dynamics and experimental measurements of mechanical properties can converge to the same length scale. Furthermore, the mechanical properties is found to be size-dependent [9, 10, 11, 12, 13] for micro- and nano-scale samples. Explaining this size-dependence presents new challenges to the existing theories as well as new opportunities for their further development.

Generally speaking, there are two approaches to probe the mechanical properties of nano-scale specimens. The most widely used approach is the bending test [14], in which a NW suspended over a trench is indented by an AFM tip until failure occurs. Yield was observed in gold NWs [10] and fracture was observed in germanium NWs beneath the indenter [15]. While this measurement is relatively easy to set up, the resulting force-displacement curve is difficult to analyse and interpret. The main difficulty comes from the unknown contact behaviour between the AFM tip and the nanowire, and the resulting high stress gradient and possible contact damage. This has made a quantitative comparison between theory and experiment very difficult.

The other approach is the tensile test. Over the last century, tensile tests were probably the most widely used method to measure the mechanical properties of bulk materials. Tensile stress-strain curves have been used to motivate, calibrate and validate various theoretical constitutive models of materials. The main reason for the popularity of tensile tests is the simplicity of the stress state throughout the entire specimen, facilitating a direct comparison with theoretical models. Unfortunately, tensile tests are difficult to perform at the nano-scale, mainly due to the challenge of manipulating the nanowire into the correct location and accurately applying and measuring the stress and strain. At this point, nano-tensile tests have been performed on carbon nanotubes where the nanotube is mounted on a MEMS device [16, 17] or between two AFM tips [18, 19]. These types of experiments are still very time consuming to set up and they have not yet been applied to long semiconductor NWs obtained from directed growth. A related approach is the

uniaxial compression test recently designed for free-standing micro-pillars [9]. Unfortunately, this design does not seem to be applicable to NWs, whose small diameter made it susceptible to buckling upon compression [20].

In this paper, we report and analyse Molecular Dynamics (MD) simulation results of Si and Ge NWs in tensile tests. We hope experimental tensile test results on semiconductor NWs will be available in the near future to compare with our theoretical predictions. The paper is organized as the following. In Section 2, we will describe our MD simulation method and the observations of NW fracture in tension. Based on these observations, we will raise three questions that will be discussed in the following sections. Section 3 will address the first question of why different potential models predict different (brittle versus ductile) behaviours. Section 4 addresses the second question of how a real Si or Ge NW would behave at room temperature. Section 5 discusses the possibility of brittle-to-ductile transition of NWs at elevated temperatures.

2 Molecular dynamics simulations

2.1 Simulation method

Experimentally, the as-grown Si and Ge NWs are typically aligned along $[111]$ or $[110]$ directions, with diameter D ranging from 10 nm to 100 nm and length well beyond $1\ \mu\text{m}$ [3, 21, 22, 23, 24]. In this study, we focus on $[110]$ oriented Si and Ge NWs. To save computational time, the NWs are relatively thin, with diameter $D = 5$ nm and length $L_z = 50$ nm, as shown in Fig. 1. Periodic boundary conditions (PBC) are applied along the wire direction to remove artificial end effects, effectively mimicking an infinitely long NW. The total number of atoms is about 50 000. The Si NW has slightly more atoms than the Ge NW because a Si atom is smaller than a Ge atom. Several inter-atomic potentials have been used in the MD simulations, including Stillinger-Weber (SW) [25, 26, 27], Tersoff [28], MEAM-Lenosky [29], and MEAM-Baskes [30]. Nose-Hoover thermostat [31, 32] is applied to maintain the temperature at $T = 300$ K. The atomic equations of motion are integrated by the Gear-6th predictor-corrector algorithm with time step $\Delta t = 0.1$ fs for Si and $\Delta t = 0.2$ fs for Ge. With these time steps, the fluctuation of the extended Hamiltonian during a 10 ps test period is on the order of 10^{-4} to 10^{-5} eV depending on the potential models. Considering that the total energy of the entire NW is on the order of 10^5 eV, this fluctuation is very small, indicating that the choice of time steps is adequate. The simulations are performed using MD++ [33].

Starting with a perfect diamond-cubic crystal, the NWs are created by removing all atoms outside a cylinder of diameter $D = 5$ nm. The atoms on the cylindrical surface are directly exposed to vacuum. The structure is first relaxed to a local energy minimum by the conjugate gradient algorithm and then equilibrated by MD at $T = 300$ K for 2 ps. The atoms on the cylindrical surface reconstruct during the initial relaxation and subsequent equilibration. The level of surface reconstruction varies for different potential models (see Appendix B.) After equilibration, the length of the simulation cell along z is increased by 1% (relative to its original length) after every 2 ps of MD simulation. This correspond to a uniaxial strain rate of $\dot{\epsilon}_{zz} = 5 \times 10^9\ \text{s}^{-1}$. The Virial stress [35] is averaged over the

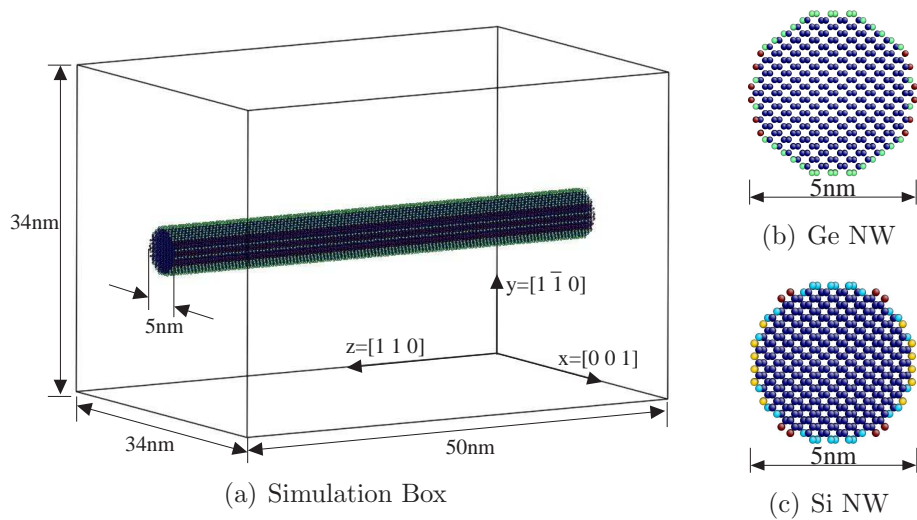


Figure 1: Simulation setup. (a) The nanowire diameter is $D = 5$ nm and its length is $L_z = 50$ nm. Periodic boundary condition is applied along the $[1\ 1\ 0]$ growth direction. (b) Cross section of the Ge NW. (c) Cross section of the Si NW. The atoms are coloured according to their local energies; the surface atoms usually have higher energy. The atomic structures are visualized by Atomeye [34].

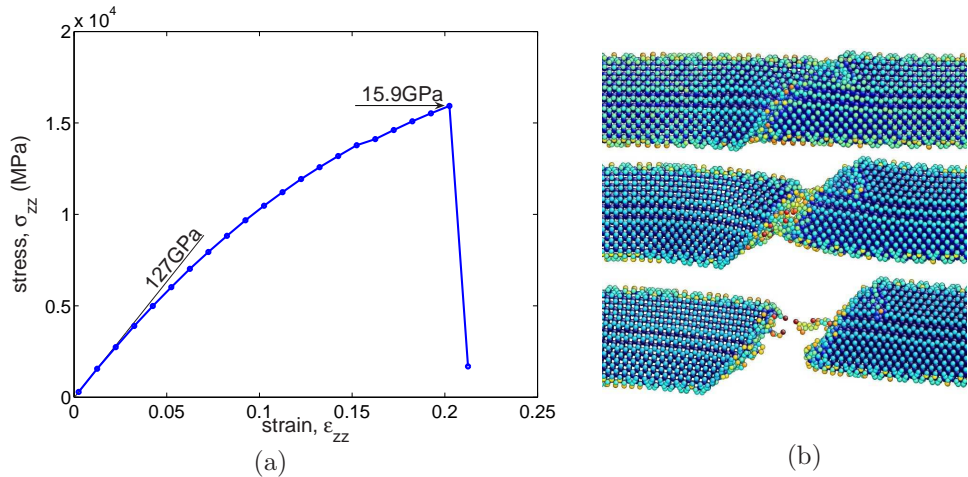


Figure 2: (a) Stress-strain curve of Ge NW under tension at $T = 300$ K in MD simulations using the SW potential. (b) Snapshots of the NW structure during fracture.

later 50% of each 2 ps period, to avoid the initial transient behaviour due to the sudden elongation of the NW. When the crack or dislocation nucleation is observed on the NW surface, we continue the simulation for another 20 ps at fixed strain to observe the fracture process.

2.2 Simulation results from SW potential

A typical simulation result is shown in Fig. 2, where (a) plots the stress-strain curve of the Ge NW described by the SW potential. The stress-strain curve is linear at small strain, the slope of which corresponds to the Young's modulus of 127 GPa. This is somewhat smaller than the Bulk Young's modulus of the same potential along $\langle 110 \rangle$ direction at zero temperature, 132 GPa, most likely due to temperature softening. At larger strain, the stress-strain relation becomes increasingly non-linear, until the stress reaches a critical value, $\sigma_{\text{frac}} = 15.9$ GPa, at which the NW fractures. The fracture stress is somewhat higher than the existing experimental estimates (between 5 and 15 GPa) [15, 18]. This may be attributed to two reasons. First, the NW in this simulation contains no surface defects whereas grown NWs may have surface roughness [36, 24] that can reduce the fracture strength. Second, the imposed strain rate in this simulation is several orders of magnitude higher than that in real experiments. This is due to the fundamental limitation on the time scale of MD simulations. Given these two reasons, the high fracture strength predicted by this simulation is not very surprising.

A detailed analysis of the atomistic structure during fracture reveals a surprising failure mechanism, as shown in Fig. 2(b). When the stress reached the critical value, sliding occurs on a $\{111\}$ plane inclined to the tensile axis. Extensive sliding over this

plane led to significant thinning of the cross section before the eventual fracture. Further analysis reveals that the first slip event was initiated by the nucleation of a dislocation half loop from the surface with Burgers vector $\mathbf{b} = \frac{1}{2}[10\bar{1}]$ on a shuffle-set (111) plane (see Fig. 7 and Fig. 10). Because extensive dislocation slip activities preceded and triggered fracture, we shall call this behaviour “ductile” fracture. Obviously, the definition of ductile fracture in a NW has some difference with that in a bulk material. Due to the small size of the NW, there can never be a macroscopic plasticity zone. Therefore, the ductile fracture here may also be called “dislocation-induced” or “slip-induced” fracture.

Because bulk Ge is a brittle material at room temperature, it is surprising that the MD simulation predicted ductile fracture for a Ge NW. Even though it is possible for a material to change its behaviour when its size is reduced to nano-scale, this prediction could also be an artifact of the empirical potential model used in the simulation. A major purpose of this paper is to distinguish the artificial effect of empirical potential models from the real size effect at the nano-scale, on the brittle versus ductile behaviour of NWs.

2.3 Simulation results from other potentials

Similar problems have been reported in fracture simulations in bulk Si using empirical potentials [37, 38, 39]. For most of the empirical potentials that have been developed for Si, including SW, a crack tip loaded in tension will not propagate (cleave), but will blunt instead, either by emitting dislocations or by amorphization, even at low temperature. This would predict bulk Si to be a ductile material, which is obviously wrong. The effect of different potential models on the behaviour of crack tips in bulk Si has been investigated. For example, it was found that, if the 3-body term in the original SW potential is multiplied by a factor of 2, it will lead to brittle (cleavage) fracture [37]. We shall refer to this modification as the SWmod potential. Obviously, this modification is *ad hoc*; it changes both the Young’s modulus (see Table 1) and the melting point of the model, as well as many other physical properties. Therefore, we cannot regard SWmod as a reliable model for Si, even though it may be argued that SW is not a reliable model for Si either, since it predicts a ductile bulk Si. The MEAM potential by Baskes [30] was found to be the most reliable potential for Si that predicts brittle fracture in the bulk [38].

To investigate the effect of potential models on the fracture behaviour of NWs, we repeated the MD simulations in the previous section with SWmod, Tersoff [28], MEAM-Lenosky [29], and MEAM-Baskes [30] potentials for both Si and Ge NWs (Lenosky potential only for Si). The stress-strain curves for Si and Ge NWs are plotted in Fig. 3 (a) and (b), respectively. The fracture strength and Young’s modulus of NWs for all potential models are listed in Table 1. Similar behaviours are observed in both Si and Ge NWs. While some potentials (e.g. SW) predict slip induced ductile fracture, as shown in Fig. 4(a), other potentials (e.g. MEAM-Baskes) predict brittle fracture by crack nucleation and propagation, as shown in Fig. 4(b). The potential models that predict ductile fracture are shaded in Table 1. There is no correlation between the predicted fracture strength and the brittle versus ductile behaviour among these potential models.

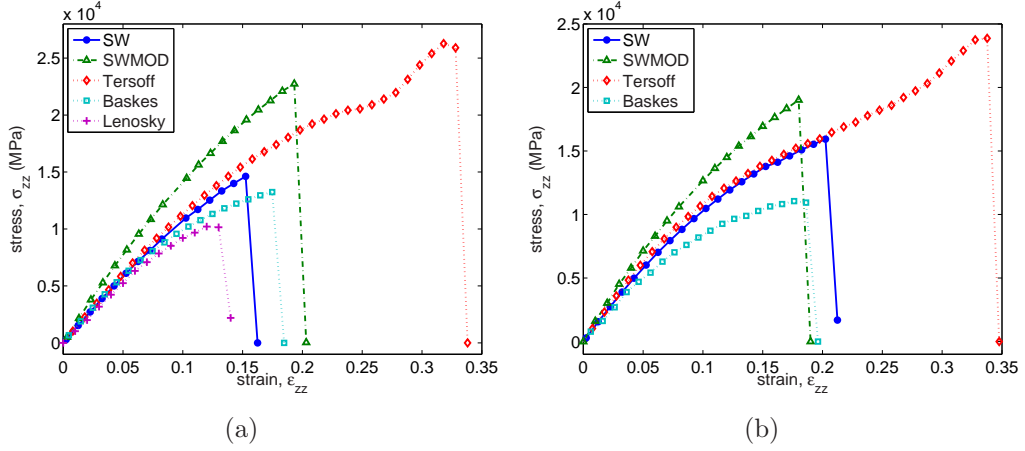


Figure 3: Stress-strain curve at $T = 300$ K for (a) Si and (b) Ge NWs from MD simulations using different potential models. Solid line with \bullet : SW; dashed-dot line with \triangle : SWmod; dotted line with \diamond : Tersoff; dotted line with \square : MEAM-Baskes; dotted line with $+$: MEAM-Lenosky.

Table 1: Fracture strengths and Young's moduli of Si and Ge NWs at $T = 300$ K with different potential models. Bulk Young's moduli at zero temperature along $\langle 110 \rangle$ direction are listed in the second to last column for comparison. All values are in units of GPa. Potential models that predict ductile fracture are shaded.

Material	Potential Model	Fracture Strength	NW Young's Modulus	Bulk Young's Modulus	Fracture Behavior
Si	SW	14.6	123	138	ductile
	Tersoff	26.3	128	138	ductile
	Lenosky	10.2	102	151	ductile
	SWmod	22.7	165	161	brittle
	Baskes	13.2	139	164	brittle
Ge	SW	15.9	127	132	ductile
	Tersoff	23.0	134	137	ductile
	SWmod	19.0	160	149	brittle
	Baskes	11.1	125	138	brittle

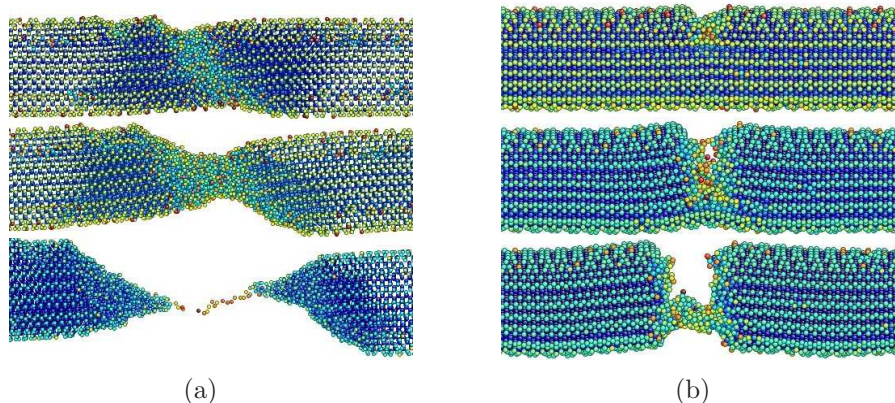


Figure 4: Snapshots of Si NW fracture in MD simulations at $T = 300$ K. (a) Slip induced ductile fracture with SW potential. (b) Crack nucleation and brittle fracture with MEAM-Baskes potential.

2.4 Fundamental questions

Given these observations from MD simulations, three questions naturally arise. First, why different potential models for the same material predict different fracture behaviours? An indication that we have found a satisfactory answer to this question would be following. Suppose that we were given a newly developed empirical potential for Si or Ge, we should be able to predict, relatively quickly, whether this potential would lead to a brittle or ductile NW, without performing the time-consuming MD simulations. Second, what is the correct behaviour for real Si and Ge NWs at room temperature? Can we make a prediction that can be compared with future experiments? Third, what are the other effects, such as temperature, NW diameter, and surface roughness, that can influence the brittle versus ductile behaviour of NWs? Bulk Si and Ge are known to have a brittle-to-ductile transition (BDT) (at temperature 600°C [40] and 400°C [41] respectively). Does BDT exist also for Si and Ge NWs? Does the small size of NWs influence the mechanism and temperature of BDT? These questions are discussed in the following sections. At this point, our answers to the first two questions are more complete than that to the third question.

3 Effect of inter-atomic potential models

3.1 Cut-off radius of inter-atomic potentials

Because most of the existing empirical potentials predicts the erroneous ductile behaviour for bulk Si, the cause of this problem must be a generic one. To this end, it is widely believed that the short cut-off radius used in most empirical potentials is responsible for the ductile behaviour. It is worth noting that the MEAM-Baskes potential, which predicts

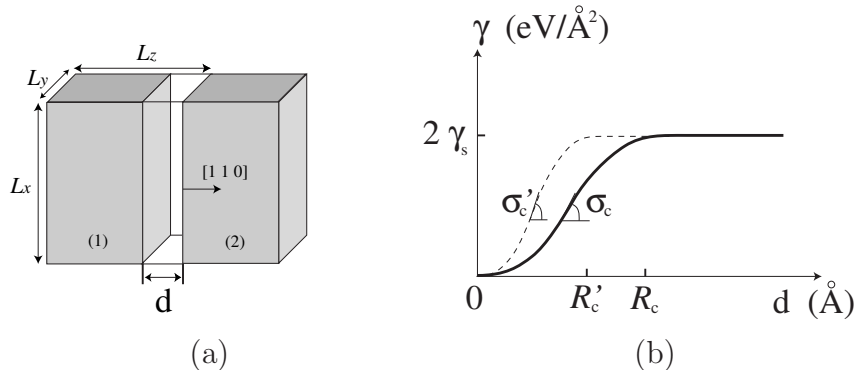


Figure 5: (a) Separating a bulk crystal across a (110) plane by distance d . (b) The excess energy per unit area γ as a result of the creation of the two new surfaces. The ideal tensile strength σ_c is defined as the maximum slope of this curve. An empirical potential with a shorter cut off radius (R'_c) would lead to a steeper slope of the $\gamma(d)$ curve and higher ideal tensile strength (σ'_c).

brittle behaviour, does have a much larger cut-off radius (6 Å) than other models that predict ductile behaviour, such as SW (3.77 Å), SWmod (3.77 Å), Tersoff (3.1 Å), and MEAM-Lenosky (4.5 Å), supporting this point of view. Incidentally, the large cut-off radius makes the MEAM-Baskes potential about 10 times more expensive to compute than the SW potential.

The rationale behind the above viewpoint is the following. Imagine the process of cutting a bulk crystal across a crystallographic plane (e.g. (110) plane) and pulling the two half-crystals apart as shown in Fig. 5(a). The total energy of the system will increase with d , the separation between the two surfaces. The excess energy per unit area of the surface, γ , is plotted as a function of d in Fig. 5(b). At sufficiently large d , $\gamma(d)$ converges to $2\gamma_s$, where γ_s is the energy density of the newly created free surfaces. The maximum slope of the $\gamma(d)$ curve has the unit of stress. It can be defined as the ideal tensile strength of the crystal along the separation direction, i.e., $\sigma_c = \max_d[\partial\gamma/\partial d]$. Performing this thought experiment on every empirical potential model, each time we will obtain a different $\gamma(d)$ curve and a different ideal tensile stress σ_c . Because the various potential models are usually fitted to reproduce roughly the same value of surface energy, γ_s , it is reasonable to expect that a potential with a shorter cut-off radius (R'_c) will produce a $\gamma(d)$ curve that rises up more steeply, leading to larger ideal tensile strength (σ'_c). If the potential model is too strong in tension, the specimen is then more likely to fail by shear, leading to ductile fracture.

3.2 Ideal tensile strength

While this argument certainly sounds plausible, it was found to be problematic upon a more quantitative analysis. Specifically, it was reported that the ideal tensile strength σ_c

Table 2: Ideal tensile strength along $[110]$ direction, ideal shear strength on (111) plane and along $[10\bar{1}]$ direction, and their ratio times the Schmid factor S , for Si and Ge for different models computed by rigid block separation at zero temperature. The Schmid factor is $S=0.4082$ (see Fig. 7(a)). The last column lists the observed fracture behaviour for NWs along $[110]$ direction in MD simulations at 300 K.

Material	Potential	Ideal tensile strength σ_c (GPa)	Ideal shear strength τ_c (GPa)	$A = S\sigma_c/\tau_c$	Observed fracture behaviour
Si	Tersoff	113	19.1	2.42	ductile
	SW	41.6	9.51	1.79	ductile
	Lenosky	33.5	11.3	1.21	ductile
	Baskes	32.0	13.9	0.940	brittle
	SWmod	41.0	19.5	0.858	brittle
	VASP/LDA	25.2	14.0	0.735	N/A
	VASP/GGA	23.0	13.7	0.685	N/A
Ge	Tersoff	93.7	11.3	3.39	ductile
	SW	30.7	11.9	1.05	ductile
	Baskes	28.2	12.1	0.951	brittle
	SWmod	30.4	17.7	0.701	brittle
	VASP/LDA	18.8	10.3	0.745	N/A
	VASP/GGA	15.6	9.87	0.645	N/A

“is not an important factor” in determining the brittle versus ductile behaviour of bulk Si models [42]. To investigate this puzzling behaviour, we compute the ideal tensile strength for all the empirical potentials.

The method for computing the ideal tensile strength is illustrated in Fig. 5(a). The rectangular simulation cell with dimension $L_x \times L_y \times L_z$ is subjected to periodic boundary conditions (PBC) in all three directions. The z -direction of the simulation cell is along $[110]$. L_z is incremented in small steps with all atoms fixed at their perfect crystal positions. This creates a gap between the crystal (1) in the primary cell with its periodic image (2). γ is simply the potential energy (in excess to that of the perfect crystal) divided by $L_x \times L_y$. The size of the simulation cell needs to be at least two times larger than the cut-off radius of the potential model. Therefore only a small number of atoms are required and the calculations are very cheap. The results are listed in Table 2. Some representative $\gamma(d)$ curves are plotted in Fig. 6. The σ_c values from different potential models span a wide range. Unfortunately, σ_c does not correlate well with the brittle or ductile behaviour observed in our MD simulations, confirming the findings reported previously [42].

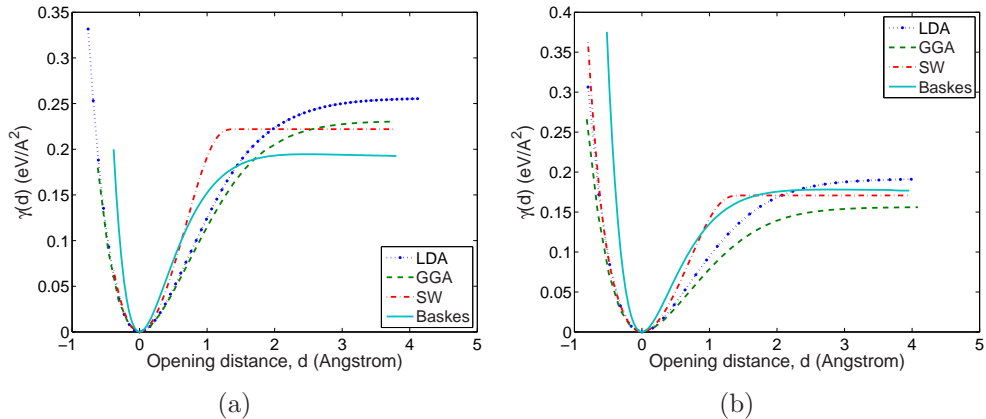


Figure 6: The (110) surface opening energy of (a) Si and (b) Ge by SW, MEAM-Baskes, and *ab initio* models.

3.3 Ideal shear strength and ductility parameter

To search for a better indicator for the brittle versus ductile behaviour of different potential models, we notice that the observed fracture behaviour is the result of the competition between two different failure modes: cleavage on (110) plane and slip on (111) plane. The ideal tensile strength σ_c measures the resistance against the former mode. Therefore, it makes sense to compute the ideal shear strength τ_c , which measures the resistance against the latter mode, and compare σ_c against τ_c . Because the slip observed in the MD simulations was initiated by the nucleation of a dislocation with Burgers vector $\mathbf{b} = \frac{1}{2}[10\bar{1}]$ on a shuffle-set (111) plane, we compute the ideal shear strength on this plane along the $[10\bar{1}]$ direction, as shown in Fig. 7(a).

The method for computing the ideal shear strength is illustrated in Fig. 7(b). The simulation cell is subjected to PBC in all three directions and initially has a rectangular shape. The repeat vector is initially along the $[111]$ direction and then tilts toward the $[10\bar{1}]$ direction by d . At the same time, the height of the simulation cell is allowed to adjust by δ , i.e.,

$$\mathbf{c}_3 = (L_z + \delta) \mathbf{n} + d \mathbf{m} \quad (1)$$

All atoms remained fixed at their perfect lattice positions, again creating a gap between the crystal (1) in the primary cell with the period image, crystal (2). For each increment of d , the potential energy of the system is minimized with respect to δ . (Incidentally, the relaxed value for δ is negative in this case.) The resulting energy, divided by $L_x \times L_y$, is usually called the (relaxed) generalized stacking fault energy, or simply γ -surface, which will be called $\tilde{\gamma}(d)$ here. $\tilde{\gamma}(d)$ is a periodic function with the periodicity of the Burgers vector. Some representative $\tilde{\gamma}(d)$ curves are plotted in Fig. 8. The maximum slope of the $\tilde{\gamma}(d)$ curve is the ideal shear strength, τ_c . The values of τ_c for all the potentials used above are listed in Table 2.

In Table 2, the ideal tensile strength σ_c is always larger than the ideal shear strength

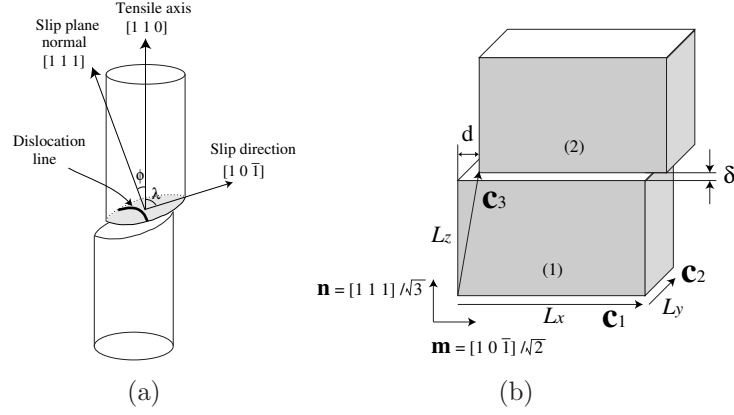


Figure 7: (a) Ductile fracture of NW is initiated by dislocation nucleation on a shuffle-set (111) plane, leading to slip in the $[10\bar{1}]$ direction. Schmid factor of this slip system is $S = \cos\phi \cos\lambda = 0.4082$, where ϕ is the angle between the tensile axis and the slip plane normal and λ is the angle between the tensile axis and the slip direction. (b) The generalized stacking fault energy for slip on a (111) plane can be computed by tilting repeat vector \mathbf{c}_3 of the simulation cell while keeping the position of all atoms fixed.

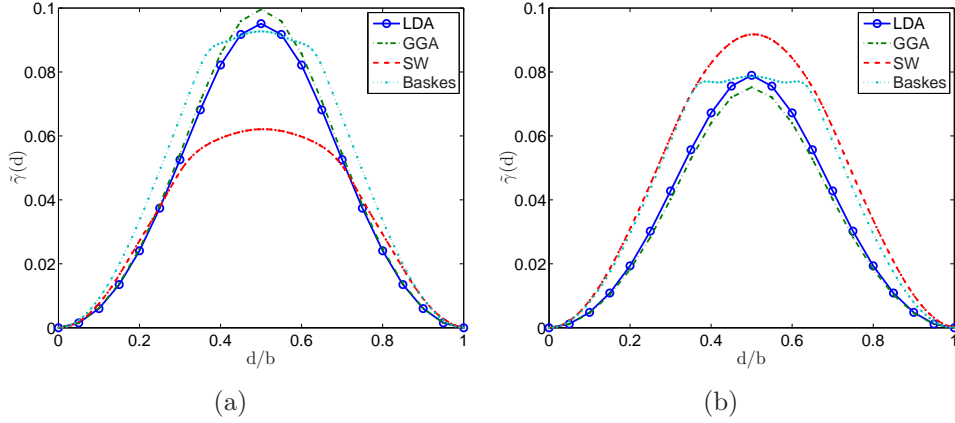


Figure 8: The generalized stacking fault energy on shuffle-set (111) plane in the $[10\bar{1}]$ direction for (a) Si and (b) Ge by SW, MEAM-Baskes and *ab initio* models. The horizontal axis is normalized by the magnitude of the Burgers vector.

τ_c . However, for a fair comparison between the two, we need to account for the Schmid factor S [43], which is the resolved shear stress on the slip system (slip plane and slip direction) per unit tensile stress.

$$S = \cos \phi \cos \lambda \quad (2)$$

where ϕ is the angle between the tensile axis and slip plane normal and λ is the angle between the tensile axis and slip direction, as shown in Fig. 7(a). For the NW geometry in this study, $S = 0.4082$. To account for the combined effect of σ_c , τ_c and S , let us define a “ductility parameter”,

$$A \equiv \frac{S\sigma_c}{\tau_c} \quad (3)$$

Intuitively, if A is very large, the material is much stronger in tension than in shear, and it will fail by ductile (slip induced) fracture. Conversely, if A is very small, the material is much stronger in shear than in tension, and it will fail by brittle (cleavage) fracture. Table 2 lists the values of the ductility parameter and shows that, $A > 1$ for all the potentials that predict ductile fracture and $A < 1$ for all the potentials that predict brittle behaviour. The agreement is surprisingly good. It shows that the parameter $A \equiv S\sigma_c/\tau_c$ is a very good indicator for the brittle versus ductile behaviour of a given potential model.

Therefore, the controversy raised previously is resolved. The ideal tensile strength alone is not a good indicator for the brittle versus ductile behaviour, but the ratio between the tensile and shear strengths is, at least for NWs. In hindsight, this conclusion may not appear surprising, as similar ideas have been used before. For example, the ratio between the ideal tensile stress σ_c and the yield stress σ_Y has been used to explain the brittle versus ductile behaviour in a continuum model of crack propagation [44]. It is worth noting that we have used a specific definition of ideal strength in our analysis, i.e. through rigid-body separation or sliding. An alternative definition of ideal strength also exists in the literature, which is the maximum stress a crystal can sustain when subjected to a uniform tensile or shear strain [45, 46]. The ideal tensile and shear strengths of different potentials according to this definition are listed in Table 4 in Appendix A. The resulting ductility parameter does not correlate well with the observed brittle or ductile behaviour of the potential model. It is reasonable that the “rigid-blocks” definition of ideal strength performs better, because when the NW fractures, significant tensile or shear strain is localized in a very small region, usually on a crystallographic plane.

Correlations have also been reported between the ductility of a materials to Poisson’s ratio, or the ratio between the shear modulus and Young’s (or bulk) modulus [47, 48, 49]. For example, brittle semiconductors have a low Poisson’s ratio, such as Si (0.218), Ge (0.200), ductile FCC metals have a high Poisson’s ratio, such as Al (0.347), Au (0.412), whereas Poisson’s ratio for BCC metals is somewhere in between, such as Fe (0.291), W (0.278)[43]. The elastic constants and Poisson’s ratios for different potentials are listed in Table 5 of Appendix A. Unfortunately, none of the ratios between elastic constants is found to correlate well with the observed brittle versus ductile behaviour in MD simulations. This means that while Poisson’s ratio can indicate the difference of ductility between different materials, it is not sensitive enough to differentiate various potential models of the same material. In summary, the ductility parameter obtained through the ideal strength of “rigid-blocks” definition out-performs alternative definitions based on similar ideas.

Table 3: Ideal tensile strength along $[1\ 1\ 1]$ direction, ideal shear strength on $(1\ 1\ \bar{1})$ plane and along $[1\ 0\ 1]$ direction, the ratio between the two times the Schmid factor S , for Si and Ge NWs along the $[1\ 1\ 1]$ direction. The Schmid factor is $S=0.2722$. Ductile or brittle fracture is predicted based on whether or not $S\sigma_c/\tau_c$ is greater or less than 1.

Material	Potential	Ideal tensile strength σ_c (GPa)	Ideal shear strength τ_c (GPa)	$A = S\sigma_c/\tau_c$	Predicted fracture behaviour
Si	Tersoff	102	19.1	1.45	ductile
	SW	38.5	9.51	1.10	ductile
	Lenosky	30.4	11.3	0.73	brittle
	Baskes	29.8	13.9	0.58	brittle
	SWmod	38.5	19.5	0.53	brittle
	VASP/LDA	22.0	14.0	0.43	brittle
	VASP/GGA	20.0	13.7	0.40	brittle
Ge	Tersoff	87.1	11.3	2.10	ductile
	SW	28.5	11.9	0.65	brittle
	Baskes	26.2	12.1	0.59	brittle
	SWmod	28.5	17.7	0.44	brittle
	VASP/LDA	17.0	10.3	0.45	brittle
	VASP/GGA	14.0	9.87	0.47	brittle

Furthermore, the simple model described above can be used to make new predictions, such as the orientation effect on the fracture behaviour of NWs. For NWs grown along the $\langle 111 \rangle$ axis, the relevant ideal tensile strength is that on the $\{111\}$ plane. The relevant ideal shear strength is still the same as before, but the Schmid factor is reduced to $S = 0.2722$. The resulting ductility parameters for different potential models are listed in Table 3. The predicted brittle versus ductile behaviours can be compared with future MD simulations. Because of the much smaller Schmid factor in this tensile orientation, most of the potential models predict brittle behaviour. Interestingly, the order of the ductility parameter among different potentials is identical compared with the $[110]$ oriented NW. Therefore, there is a consistent trend suggesting that $[111]$ oriented Si and Ge NWs are more brittle than $[110]$ oriented NWs.

4 Beyond empirical potential models

Having examined why a given potential model predicts brittle or ductile fracture, we now turn to the second question: what is the correct fracture behaviour of a real Si (or Ge) NW? After all, there is only one Si (or Ge) in nature, even though many potential models have been developed for it. While experimental observation may be the only way to obtain a final answer, we would like to make a theoretical prediction *before* the experiment, which would enable a more meaningful comparison between the theory and the experiment.

In order to go beyond the limited accuracy of empirical potential models, we resort to the *ab initio* method based on the density functional theory (DFT). We use the Vienna ab-initio simulation package (VASP) [50] with the local density approximation (LDA) as well as the generalized gradient approximation (GGA). The Ultra-soft pseudopotential is used for Si-LDA calculations, and the projector augmented-wave (PAW) method [51, 52] is used for the rest, including Si-GGA, Ge-LDA, and Ge-GGA. The k -points are sampled by a $4 \times 4 \times 4$ Monkhorst-Pack method and the cut-off energy for the plane wave is 22.05 Ry. The ideal tensile strengths by rigid-block separation are computed using a simulation cell of $4[110] \times [\bar{1}10] \times [001]$, containing 64 atoms. The ideal shear strengths are computed using a simulation cell of $2[111] \times [10\bar{1}]/2 \times [\bar{1}2\bar{1}]/2$, containing 24 atoms. More atoms are used in ideal tensile strength calculations, in order to make sure that the large surface separations do not affect the convergence of numerical results.

Ab initio results of the ideal tensile and shear strengths by the “rigid-body” separation and sliding are listed in Table 2. The corresponding ductility parameter, $A = S\sigma_c/\tau_c$, is 0.735 for Si and 0.745 for Ge. Based on the correlation between this parameter and the MD observations, the *ab initio* data predict that Si and Ge NWs will fail in tension by brittle fracture at room temperature. It is interesting to note that the *ab initio* models of Si are somewhat “more brittle” than the MEAM-Baskes model, in that its ductility parameter is even lower. Compared with the *ab initio* models, the Baskes model of Si gives a very accurate ideal shear strength, but overestimates the ideal tensile strength. At the same time, it seems that the SWmod model predicts brittle fracture “for the wrong reason”, in that it overestimates both the ideal tensile and shear strengths, compared with the *ab initio* models.

Given the relative ease of ideal tensile and shear strength calculations, we propose

that they should be performed for future potential models of semiconductors. If the ideal strengths, especially the ratio between tensile and shear strengths, are too different from *ab initio* values, then the applicability of this potential to fracture related simulations is poor. To facilitate these calculations, we have posted MD++ and the script files for computing the ideal strengths on our web site [33].

5 Brittle-to-ductile transition

5.1 Limitations of ductility parameter

While we have so far focused on the “artificial” effect of different potential models, in this section we begin to address some “real” effects of physical parameters, such as temperature, on the fracture behaviour of NWs. In hindsight, the very good agreement between the ductility parameter, $S\sigma_c/\tau_c$, and the observed fracture behaviour, as shown in Table 2, is somewhat surprising for the following reasons.

First, the ideal strengths, σ_c and τ_c , are computed by separating or sliding two crystals rigidly; the atom positions are not allowed to fluctuate or relax, hence corresponding to the zero-temperature behaviour. On the contrary, the MD simulations of NW fracture are performed at $T = 300$ K. Yet the ratio between σ_c and τ_c still correlates well with the brittle versus ductile behaviour observed in MD simulations. A possible explanation is that 300 K is still in the low-temperature regime, which means that at higher temperatures, the behaviour observed in MD simulations is expected to deviate from that predicted by the simple ductility parameter. Indeed, bulk Si has a brittle-to-ductile transition (BDT) at 600°C (Ge at 400°C) [40, 41]. It is reasonable to expect that Si (or Ge) NWs, now predicted to be brittle at room temperature, may also have a BDT at higher temperatures.

Second, the ideal strengths have been computed with periodic boundary conditions (PBC) in all 3 directions, thus corresponding to the bulk behaviour, while we have been using them to discuss the fracture behaviour of NWs. The NW surface, which is absent in ideal strength calculations, is playing an important role in MD simulations. NW fracture, either by cleavage or by sliding, does not occur homogeneously on a cross-sectional plane; instead it is always initiated by a heterogeneous nucleation from the surface, see e.g. Fig. 9 and Fig. 10. Correspondingly, the fracture strength σ_{frac} observed in MD simulations (Table 1) is always lower than the ideal tensile strength, σ_c (for brittle fracture) or the ideal shear strength divided by the Schmid factor, τ_c/S (for ductile fracture, Table 2). The small size of the NW could have an effect on the dislocation or crack nucleation at the surface and influence the BDT if it exists.

5.2 MD observations

To investigate the possibility of BDT for NWs, we repeat the MD simulations of Si NW in tension at 600 K, 900 K and 1200 K. The MEAM-Baskes potential is used, because its ideal strengths are the closest to those from the *ab initio* model, and because it predicts brittle fracture at room temperature. Cleavage fracture is observed at 600 K (not shown here), similar to that at 300 K. But the fracture behaviour at 900 K is different. As

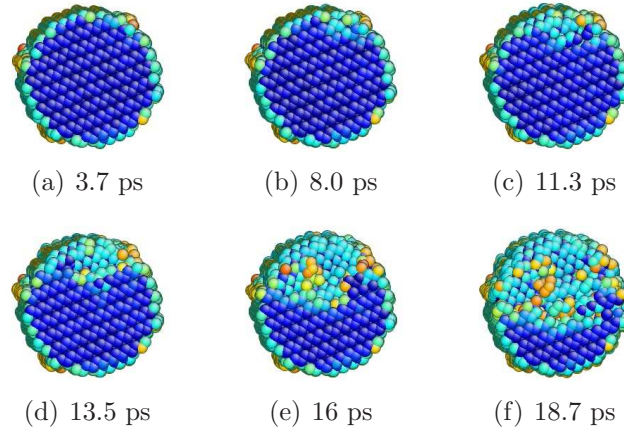


Figure 9: (colour) Snapshots of MD simulation of Si NW fracture at 300 K by the SWmod potential. The crack initiates from the surface of NW in (b) and propagates along the cross-sectional (110) plane in (c)-(f). The atoms are coloured by their local energy. The times elapsed since the application of 20% strain are listed beneath the figures.

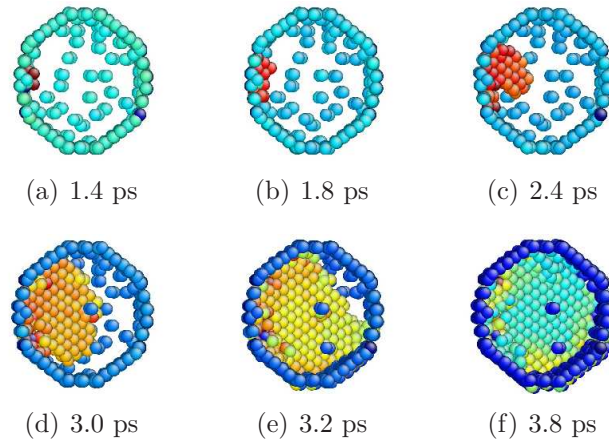


Figure 10: (colour) Snapshots of MD simulation of Ge NW fracture at 300 K by the SW potential. The dislocation nucleates from the surface of the NW in (a) and propagates along the (111) plane in (b)-(e), eventually creating a surface step in (f). The atoms are coloured by the current distance from their neighbor in the initial (reference) configuration. The times elapsed since the application of 21% strain are listed beneath the figures.

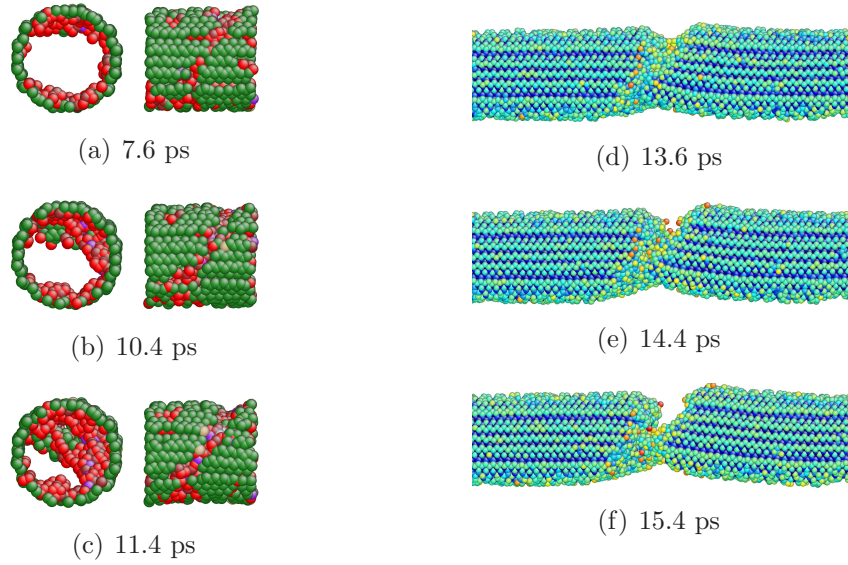


Figure 11: (colour) Snapshots of MD simulations of Si NW fracture at 900 K by the MEAM-Baskes potential. (a) Slip initiates on a (111) plane but is confined close to the surface. In (b) and (c), the slip penetrates into the NW. As a result, large wedge is visible in (c) on the NW surface. Further slip leads to necking in (d). Due to the stress concentration, a crack is nucleated beneath the wedge in (d) and become visible in (e). NW fractures in (f). In (a)-(c) atom are coloured by local coordinate number and atoms with coordinate number 4 are not plotted. Atoms in (d)-(f) are coloured by local energy. The times elapsed since the application of 14% strain are listed beneath the figures.

shown in Fig. 11, failure is initiated as slip on a (1 1 1) surface inclined to the tensile axis. Interestingly, the propagation of slip is different from that observed in low temperature simulations using the SW potential (Fig. 10). Instead of simply propagate from one side of the cross section to the other side, the slip area is initially confined close to the surface, assuming the shape of a horseshoe (Fig. 11(b)), and then gradually penetrates into the NW. Significant sliding leads to the formation of a wedge on the surface. The resulting stress concentration eventually leads to a crack nucleation and NW fracture. Compared with the behaviour at 300 K, the NW failure appears much more ductile, because of a significant amount of slip. However, the slip behaviour is not as clear-cut as those observed in 300 K simulations using the SW potential. Instead complex interaction between slip and crack is observed at 900 K using the MEAM-Baskes potential. MD simulations at 1200 K (not shown here) show even more pronounced slip activities before NW fracture. Therefore, these simulation results suggest a more gradual transition from brittle fracture to ductile fracture with increasing temperature, instead of a sharp BDT observed in bulk Si. Our predictions are likely to have been influenced by the very high strain rate used in these simulations. Reducing the strain rate should lead to a lower transition temperature.

A detailed analysis of the BDT mechanism in NWs will be presented in a future paper. Here we make a few general remarks based on the simulation data presented above. Given the two failure modes repeatedly observed in these MD simulations, the BDT is most likely the result of the competition between the nucleation of a crack and the nucleation of a dislocation, both from the surface. We have established, from *ab initio* calculations, that in the zero-temperature limit, the critical stress to induce cleavage fracture is lower than the critical stress to induce slip. When the applied stress is below the critical stress, thermal fluctuation is needed to over the energy barrier for the crack or dislocation nucleation. At very low temperature, the energy barrier for crack nucleation must be smaller than that for dislocation nucleation. But the balance may change at higher temperatures, leading to a brittle-to-ductile transition.

Even though the details of BDT mechanism in NWs is not yet clear, it should be different from the BDT mechanism for the bulk. While many different models of BDT in bulk Si have been proposed, the starting point has always been a pre-existing macro-crack. Brittle or ductile behaviour is linked to whether the crack tip will propagate or will emit dislocations under external loading [53, 54, 55, 56, 57, 58, 59, 60, 61, 62]. This type of models does not apply to NWs. Due to their small size, NWs do not contain a macro-crack at all. Instead, the crack has to be nucleated from the surface for brittle fracture to occur. Therefore, BDT in NWs is determined by the competition between two *nucleation* processes, in the absence of a pre-existing crack. While the surface roughness and surface stress on NWs may facilitate crack and dislocation nucleation, their effect is quite different from that of a macro-crack in a bulk crystal. The different BDT mechanism in NWs may lead to a different BDT temperature and the transition may be more gradual than that in the bulk. This presents an interesting opportunity to compare theoretical predictions and experimental measurements with each other. Because NWs with different orientations have different ductility parameters (Table 2 v.s. Table 3), they may also have different BDT temperatures. When compared to future experiments, the predictions made here are probably more relevant for Ge NWs, because Si NWs are usually covered by a layer of oxides, which is neglected in our simulations. Surface oxidization and reconstruction are

also expected to influence the BDT of NWs and these effects will be discussed in a future paper.

6 Summary

We have performed MD simulations on the fracture of Si and Ge NWs in tension along the $[110]$ direction at room temperature, using a set of empirical potential models. While some potentials show brittle fracture by crack nucleation, other potentials show ductile fracture by dislocation nucleation. A ductility parameter is introduced, which is the ideal tensile strength over the ideal shear strength, multiplied by the Schmid factor. The magnitude of the ductility parameter compared to one exhibits perfect agreement with whether ductile or brittle fracture is observed in the MD simulations. The ductility parameter has been computed by *ab initio* models, which predicts brittle fracture at room temperature. Our model also predicts that $[111]$ -oriented NWs should be more brittle than $[110]$ -oriented NWs.

While the MEAM-Baskes potential predicts brittle fracture at 300 K and 600 K, significant slip activities are observed in MD simulations at 900 K and 1200 K using the same potential. It seems to be very useful to study the BDT of semiconductor NWs by both theory and experiments, and to compare their results with each other. The main benefits of NWs is that comparison between theory and experiments can be made on the same length scale. If quantitative agreement between theory and experiment can be obtained for NWs, the findings should be useful to elucidate the BDT mechanisms in bulk semiconductors.

Acknowledgement

We appreciate the kind help from Dr. M. I. Baskes, who provided us the source codes of the MEAM potential. We would like to thank Prof. W. D. Nix and Prof. J. K. Hsia for helpful discussions, Dr. B. Sadigh for helping us with the Lenosky potential, and Dr. J. Marian for helping us with the MEAM potential. We would also like to thank Prof. H. Dai and Dr. R. Grow for stimulating our interest in the fracture of semiconductor NWs by sharing with us their experimental data on NW bending and fracture. This work is partly supported by an NSF grant CMS-0556032.

References

- [1] Y. Cui, L. J. Lauhon, M. S. Gudiksen, J. Wang, and C. M. Lieber. Diameter-controlled synthesis of single-crystal silicon nanowires. *Applied Physics Letters*, 78:2214–2216, 2001.
- [2] K. Byon, D. Tham, and J. E. Fischer. Synthesis and postgrowth doping of silicon nanowires. *Appl. Phys. Lett.*, 87:193104–1–3, 2005.
- [3] Y. Cui, Z. Zhong, D. Wang, W. U. Wang, and C. M. Lieber. High performance silicon nanowire field effect transistors. *Nano Letters*, 3:149–152, 2003.

- [4] D. Wang, Q. Wang, A. Javey, R. Tu, and H. Dai. Germanium nanowire field-effect transistors with SiO₂ and high- κ HfO₂. *Appl. Phys. Lett.*, 83:2432–2434, 2003.
- [5] Y. Huang and C. M. Lieber. Integrated nanoscale electronics and optoelectronics: Exploring nanoscale science and technology through semiconductor nanowires. *Pure Appl. Chem*, 76:2051–2068, 2004.
- [6] Y. Cui, Q. Wei, H. Park, and C. M. Lieber. Nanowire nanosensors for highly sensitive and selective detection of biological and chemical species. *Science*, 293:1289–1292, 2001.
- [7] M. Chau, O. Englander, and L. Lin. Silicon nanowire-based nanoactuator. In *Proceedings of the 3rd IEEE conference on nanotechnology*, volume 2, pages 879–880, San Francisco, CA, Aug 12-14 2003.
- [8] R. Fan, R. Karnik, M. Yue, D. Y. Li, A. Majumdar, and P. D. Yang. DNA translocation in inorganic nanotubes. *Nano Letters*, 5:1633–1637, 2005.
- [9] M. D. Uchic, D. M. Dimiduk, J. N. Florando, and W. D. Nix. Sample dimensions influence strength and crystal plasticity. *Science*, 305:986–989, 2004.
- [10] B. Wu, A. Heidelberg, and J. J. Boland. Mechanical properties of ultrahigh-strength gold nanowire. *Nature Mater.*, 4:525–529, 2005.
- [11] R. E. Miller and V. B. Shenoy. Size-dependent elastic properties of nanosized structural elements. *Nanotechnology*, 11:139–147, 2000.
- [12] S. Cuenot, C. Frétigny, S. Demoustier-Champagne, and B. Nysten. Measurement of elastic modulus of nanotubes by resonant contact atomic force microscopy. *J. Appl. Phys.*, 93:5650–5655, 2003.
- [13] K. Gall, J. Diao, and M. L. Dunn. The strength of gold nanowires. *Nano Lett.*, 4:2431–2436, 2004.
- [14] A. San Paulo, J. Bokor, R. T. Howe, R. He, P. Yang, D. Gao, C. Carraro, and R. Maboudian. Mechanical elasticity of single and double clamped silicon nanobeams fabricated by the vapor-liquid-solid method. *Appl. Phys. Lett.*, 87:053111, 2005.
- [15] R. Grow and H. Dai. unpublished results on Ge nanowire bending test, 2005.
- [16] Y. Zhu and H. D. Espinosa. An electromechanical material testing system for *in situ* electron microscopy and applications. *Proc. Nat'l. Acad. Sci.*, 102:14503–14508, 2005.
- [17] Y. Isono, M. Kiuchi, and S. Matsui. Development of electrostatic actuated nano tensile testing device for mechanical and electrical characteristics of FIB deposited carbon nanowire. presented at the 2006 MRS spring meeting, San Francisco, CA, 2006.
- [18] T. Kizuka, Y. Takatani, K. Asaka, and R. Yoshizaki. Measurements of the atomistic mechanics of single crystalline silicon wires of nanometer width. *Phys. Rev. B*, 72:035333–1–6, 2005.

- [19] W. Ding, L. Calabri, X. Chen, K. Kohlhass, and R. S. Ruoff. Mechanics of crystalline boron nanowires. presented at the 2006 MRS spring meeting, San Francisco, CA, 2006.
- [20] N. A. Melosh. Personal communications.
- [21] J. D. Holmes, K. Johnston, R. C. Doty, and B. A. Korgel. Control of thickness and orientation of solution-grown silicon nanowires. *Science*, 287:1471, 2000.
- [22] D. Wang and H. Dai. Low-temperature synthesis of single-crystal germanium nanowires by chemical vapor deposition. *Angew. Chem. Int. Ed.*, 41:4783–4786, 2002.
- [23] H. Jagannathan, M. Deal, Y. Nishi, J. Woodruff, C. Chidsey, and P. C. McIntyre. Nature of germanium nanowire heteroepitaxy on silicon substrates. *J. Appl. Phys.*, 100:024318, 2006.
- [24] H. Adhikari, A. F. Marshall, C. E. D. Chidsey, and P. C. McIntyre. Germanium nanowire epitaxy: Shape and orientation control. *Nano Letters*, 6:318 – 323, 2006.
- [25] F. H. Stillinger and T. A. Weber. Computer simulation of local order in condensed phase of silicon. *Phys. Rev. B*, 31:5262–5271, 1985.
- [26] H. Balamane, T. Halicioglu, and W. A. Tiller. Comparative study of silicon empirical interatomic potentials. *Phys. Rev. B*, 46:2250–2279, 1992.
- [27] K. Ding and H. C. Andersen. Molecular-dynamics simulation of amorphous germanium. *Phys. Rev. B*, 34:6987–6991, 1986.
- [28] J. Tersoff. Modeling solid-state chemistry: Interatomic potentials for multicomponent systems. *Phys. Rev. B*, 39:5566–5568, 1989.
- [29] T. J. Lenosky, B. Sadigh, E. Alonso, V. V. Bulatov, T. Diaz de la Rubia, J. Kim, A. F. Voter, and J. D. Kress. Highly optimized empirical potential model of silicon. *Model. Simul. Mater. Sci. Eng.*, 8:825–841, 2000.
- [30] M. I. Baskes. Modified embedded-atom potentials for cubic materials and impurities. *Phys. Rev. B*, 46:2727–2742, 1992.
- [31] S. Nosé. A molecular dynamics method for simulations in the canonical ensemble. *Molecular Physics*, 52:255–268, 1984.
- [32] W. G. Hoover. Canonical dynamics: Equilibrium phase-space distributions. *Phys. Rev. A*, 31:1695–1697, 1985.
- [33] MD++ code is available at <http://micro.stanford.edu/~caiwei/Forum>.
- [34] J. Li. Atomeye: an efficient atomistic configuration viewer. *Modell. Simul. Mater. Sci. eng.*, 11:173–177, 2003. Atomeye can be downloaded from the website <http://164.107.79.177/Archive/Graphics/A/>.
- [35] G. Marc and W. G. McMillan. The virial theorem. In I. Prigogine and S. A. Rice, editors, *Advances in Chemical Physics*, volume 58, pages 209–361. Interscience, 1985.
- [36] L. J. Lauhon, M. S. Gudiksen, D. Wang, and C. M. Lieber. Epitaxial core-shell and core-multishell nanowire heterostructures. *Nature*, 420:57–61, 2002.

- [37] J. A. Hauch, D. Holland, M. P. Marder, and H. L. Swinney. Dynamic fracture in single crystal silicon. *Phys. Rev. Lett.*, 82:3823–3826, 1999.
- [38] N. P. Bailey and J. P. Sethna. Macroscopic measure of the cohesive length scale: Fracture of notched single-crystal silicon. *Phys. Rev. B*, 68:205204, 2003.
- [39] M. Marder. Molecular dynamics of cracks. *Comput. Sci. Eng.*, 1:48–55, 1999.
- [40] J. Samuels and S. G. Roberts. The brittle-ductile transition in silicon. i. experiments. *Proc. Roy. Soc. Lond. A*, 421:1–23, 1989.
- [41] F. C. Serbena and S. G. Roberts. The brittle-ductile transition in germanium. *Acta Metall. Mater.*, 42:2505–2510, 1994.
- [42] J. G. Swadener, M. I. Baskes, and M. Nastasi. Molecular dynamics simulation of brittle fracture in silicon. *Phys. Rev. Lett.*, 89:085503, 2002.
- [43] J. P. Hirth and J. Lothe. *Theory of Dislocations*. Krieger Publishing Company, 2nd reprinted edition, 1992.
- [44] V. Tvergaard and J. W. Hutchinson. The relation between crack growth resistance and fracture process parameters in elastic-plastic solids. *J. Mech. Phys. Solids*, 40:1377–1397, 1992.
- [45] D. Roundy and M. L. Cohen. Ideal strength of diamond, Si and Ge. *Physical Review B*, 64:212103, 2001.
- [46] S. Ogata, J. Li, and S. Yip. Ideal pure shear strength of aluminium and copper. *Science*, 298:807–811, 2002.
- [47] S. S. Hecker, D. L. Rohr, and D. F. Stein. Brittle fracture in iridium. *Metall. Trans. A*, 9A:481–488, 1978.
- [48] S. F. Pugh. Relations between elastic moduli and plastic properties of polycrystalline pure metals. *Philos. Mag.*, 45:823–843, 1954.
- [49] J. J. Lewandowski, W. H. Wang, and A. L. Greer. Intrinsic plasticity or brittleness of metallic glasses. *Philos. Mag. Lett.*, 85:77–87, 2005.
- [50] The Vienna Ab initio Simulation Package (VASP). <http://cms.mpi.univie.ac.at/vasp/>.
- [51] P. E. Blöchl. Projector augmented-wave method. *Phys. Rev. B*, 50:17953–17979, 1994.
- [52] G. Kresse and D. Joubert. From ultrasoft pseudopotentials to the project augmented-wave method. *Phys. Rev. B*, 59:1758–1775, 1999.
- [53] J. R. Rice and R. Thomson. Ductile versus brittle behaviour of crystals. *Philos. Mag.*, 29:73 – 97, 1974.
- [54] J. R. Rice. Dislocation nucleation from a crack tip: an analysis based on the peierls concept. *J. Mech. Phys. Solids*, 40:239 – 71, 1992.

- [55] J. R. Rice and G. E. Beltz. The activation energy for dislocation nucleation at a crack. *J. Mech. Phys. Solids*, 42:333 – 60, 1994.
- [56] J. Samuels, S. G. Roberts, and P. B. Hirsch. The brittle-to-ductile transition in silicon. *Mater. Sci. Eng. A*, 105/106:39 – 46, 1988.
- [57] S. G. Roberts, M. Ellis, and P. B. Hirsch. Dislocation dynamics and brittle-to-ductile transitions. *Mater. Sci. Eng. A*, 164:135 – 40, 1993.
- [58] M. Brede, K. J. Hsia, and A. S. Argon. Brittle crack propagation in silicon single crystals. *J. Appl. Phys.*, 70:758 – 771, 1991.
- [59] V. R. Nitzsche and K. J. Hsia. Modelling of dislocation mobility controlled brittle-to-ductile transition. *Mater. Sci. Eng. A*, 176:155 – 164, 1994.
- [60] A. S. Argon and K. I. Hsia. Experimental study of the mechanisms of brittle-to-ductile transition of cleavage fracture in Si single crystals. *Mater. Sci. Eng. A*, 176:111 – 119, 1994.
- [61] A. S. Argon, G. Xu, and M. Ortiz. Kinetics of dislocation emission from crack tips and the brittle to ductile transition of cleavage fracture. *Mater. Res. Soc. Symp. Proc.*, 409:29 – 44, 1996.
- [62] G. Xu, A. S. Argon, and M. Ortiz. Critical configurations for dislocation nucleation from crack tips. *Philos. Mag. A*, 75:341 – 67, 1997.

A Alternative ductility indicators

Here we examine the effectiveness of alternative definition of the ductility parameter based on the same idea of the competition between tension and shear. The first alternative is based on the ideal strengths defined in terms of uniform strain, the maximum stress in a crystal that is subjected to a uniform extension or shear. The results are shown in Table 4. The second alternative is based on the ratio between elastic constants, e.g. shear and Young’s modulus. The results are shown in Table 5. Unfortunately, the correlation between these alternative ductility indicators with observed brittle versus ductile behaviour are not as good as that based on ideal strength by “rigid-body” sliding.

Table 4: Ideal strength of different potentials obtained by applying a uniform tensile or shear strain to a crystal. The tensile axis is along $[1\ 1\ 0]$ direction and the shear is on (111) plane and along $[1\ 1\ 0]$ direction. The relative position between the two atoms in the basis of the diamond-cubic crystal is allowed to relax. The correlation between the observed brittle versus ductile behaviour in MD simulations and the ductility parameter breaks down for the SWmod potential.

Material	Potential	Ideal tensile strength σ_c (GPa)	Ideal shear strength τ_c (GPa)	$S\sigma_c/\tau_c$	Observed fracture behaviour
Si	Tersoff	117	18.0	2.66	ductile
	SW	42.1	10.6	1.62	ductile
	Lenosky	36.7	9.5	1.58	ductile
	Baskes	22.0	10.5	0.86	brittle
	SWmod	42.0	13.1	1.31	brittle
Ge	Tersoff	96.0	13.4	2.93	ductile
	SW	30.6	11.0	1.14	ductile
	Baskes	17.3	9.0	0.78	brittle
	SWmod	30.6	13.0	0.96	brittle

Table 5: Elastic constants and their ratios for different potential models. C_{11} , C_{12} and C_{44} are the three fundamental elastic constants expressed in the cubic coordinate system, from which all other entries in this Table are calculated. ν_1 and ν_2 are the two Poisson's ratio and Y is the Young's modulus for tension along the $[1\ 1\ 0]$ axis. Specifically, $\nu_1 = -S_{3311}/S_{3333}$, $\nu_2 = -S_{3322}/S_{3333}$, and $Y = 1/S_{3333}$, where S is the elastic compliance tensor expressed in the coordinate system formed by $\mathbf{e}_1 = [0\ 0\ 1]$, $\mathbf{e}_2 = [1\ \bar{1}\ 0]$, and $\mathbf{e}_3 = [1\ 1\ 0]$. Y 's for empirical potentials are listed in Table 1. $\mu = C'_{1212}$ is the shear modulus, where C' is the elastic stiffness tensor expressed in the coordinate system formed by $\mathbf{e}'_1 = [1\ 0\ \bar{1}]$, $\mathbf{e}'_2 = [1\ 1\ 1]$, and $\mathbf{e}'_3 = [1\ \bar{2}\ 1]$. B is the bulk modulus. Experimental data are for $T = 300$ K [43]. None of the ratios between the elastic constants correlates well with the brittle versus ductile (shaded) behaviour observed in MD simulations.

Potential	C_{11}	C_{12}	C_{44}	ν_1	ν_2	μ	B	μ/B	μ/Y	
Si	SW	161	80.5	60.2	0.428	1.44e-1	46.9	108	0.434	0.340
	Tersoff	141	74.0	68.9	0.526	1.72e-3	45.3	98.1	0.462	0.329
	Lenosky	164	83.0	70.5	0.469	7.23e-2	50.5	110	0.459	0.334
	SWmod	161	80.5	80.4	0.500	-6.22e-4	53.6	108	0.497	0.333
	Baskes	161	63.3	76.9	0.368	6.31e-2	58.2	97.6	0.596	0.356
	LDA	159	67.3	80.0	0.411	2.83e-2	57.2	97.9	0.585	0.348
	GGA	151	60.6	79.2	0.396	1.42e-2	56.5	90.6	0.624	0.352
	Exp't	165.7	63.9	79.6	0.362	6.22e-2	60.5	97.8	0.618	0.465
Ge	SW	137	50.1	58.7	0.321	1.23e-1	48.5	80.0	0.607	0.368
	Tersoff	137	43.4	61.9	0.283	1.05e-1	51.8	75.7	0.685	0.379
	SWmod	137	50.1	73.8	0.362	9.59e-3	53.6	79.9	0.670	0.359
	Baskes	127	47.4	68.8	0.371	5.13e-3	49.5	75.2	0.658	0.358
	LDA	127	44.8	63.1	0.334	5.25e-2	48.4	72.3	0.670	0.364
	GGA	103	39.0	54.0	0.371	2.03e-2	39.3	60.4	0.651	0.357
	Exp't	128.9	48.3	67.1	0.365	2.47e-2	49.2	75.2	0.655	0.480

B Surface Reconstruction

During the preparation of the NW specimens for MD simulations, we observe reconstruction of surface atoms for all the potential models used in this study. The NW specimens are prepared in two steps. The first step is the conjugate gradient energy minimization starting from a “freshly-cut” cylinder out of a perfect crystal. In the second step, the relaxed structure is used as initial condition for MD simulations at 300 K at zero stress by 2 ps and then relaxed by conjugate gradient method again. The latter relaxation is performed to remove the thermal noise at finite temperature. To quantify the amount of reconstruction, we measure the maximum displacement of all atoms and the change of total energy in each of these two steps. The results for all the potential models are listed in Table 6.

The SW and SWmod potentials do not show any reconstruction at all during the first step (relaxation at zero temperature), but surface reconstruction does occur spontaneously during the equilibration at 300 K. On the other hand, the Baskes (MEAM) potential shows significant reconstruction in the first step, but smaller change in the second step than other potentials. The behavior of the Tersoff and Lenosky (MEAM) potentials lies somewhere in between these two cases.

Table 6: The maximum displacement d_{\max} of surface atoms of Si NW and the total energy change ΔE_{tot} during initial relaxation at 0 K and subsequent equilibration at 300 K.

Potential	Relaxation at 0 K		Equilibration at 300 K	
	$d_{\max}(\text{\AA})$	$\Delta E_{\text{tot}} \text{ (eV)}$	$d_{\max}(\text{\AA})$	$\Delta E_{\text{tot}} \text{ (eV)}$
SW	8.6923e-6	-7.5402e-7	4.5534e+0	-2.8685e+3
SWmod	7.2383e-6	-7.0399e-7	4.1784e+0	-2.1299e+3
Tersoff	1.7576e-1	-2.3218e+2	2.8568e+0	-1.0446e+3
Lenosky	4.4693e-2	-2.7991e+1	6.1451e+0	-2.9507e+3
Baskes	9.6444e-1	-2.1608e+3	1.7871e+0	3.5841e+0